



UNIVERSITY OF LEEDS

This is a repository copy of *Mechanistic Insights of Dissolution and Mechanical Breakdown of FeCO₃ Corrosion Films*.

White Rose Research Online URL for this paper:
<https://eprints.whiterose.ac.uk/170443/>

Version: Accepted Version

Article:

Matamoros Veloza, A orcid.org/0000-0002-3870-9141, Barker, R, Vargas, S et al. (1 more author) (2021) Mechanistic Insights of Dissolution and Mechanical Breakdown of FeCO₃ Corrosion Films. ACS Applied Materials and Interfaces. ISSN 1944-8244

<https://doi.org/10.1021/acsami.0c18976>

© 2021 American Chemical Society. This is an author produced version of an article published in ACS Applied Materials and Interfaces. Uploaded in accordance with the publisher's self-archiving policy.

Reuse

Items deposited in White Rose Research Online are protected by copyright, with all rights reserved unless indicated otherwise. They may be downloaded and/or printed for private study, or other acts as permitted by national copyright laws. The publisher or other rights holders may allow further reproduction and re-use of the full text version. This is indicated by the licence information on the White Rose Research Online record for the item.

Takedown

If you consider content in White Rose Research Online to be in breach of UK law, please notify us by emailing eprints@whiterose.ac.uk including the URL of the record and the reason for the withdrawal request.



eprints@whiterose.ac.uk
<https://eprints.whiterose.ac.uk/>

Mechanistic insights of dissolution and mechanical breakdown of FeCO₃ corrosion films

Adriana Matamoros-Veloza^a, Richard Barker^a, Silvia Vargas^b, Anne Neville^a

^a Institute of Functional Surfaces, School of Mechanical Engineering, University of Leeds, Leeds, LS2 9JT, UK

^b BP America, Inc., Houston, Texas 77079, United States

Abstract

Carbon steel is a universally used material in various transportation and construction industries. Research related to CO₂ corrosion environments agree on the occurrence of siderite (FeCO₃) as a main product conforming corrosion films, suggested to impart protection to carbon steel. Identifying and understanding the presence of all corrosion products under certain conditions is of greatest importance to elucidate the behavior of corrosion films under operation conditions (e.g., flow, pH, temperature) but information regarding the nature and formation of other Fe corrosion products apart from FeCO₃ is lacking. Corrosion products in CO₂ environments typically consist of common Fe minerals that in nature have been demonstrated to undergo transformations forming other Fe phases. This fact of nature has not been yet explored in the corrosion science field, which can help us to describe mechanisms associated to industrial processes. In this work, we present a multiscale and multidisciplinary approach to understand the mechanisms occurring on corrosion films under the key factors of flow and pH through the combination of molecular techniques with imaging. We report that certainly siderite (FeCO₃, cylindrical with trigonal-pyramidal caps) is the main product identified under the conditions used (representative of brine transport at 80°C) but wustite (FeO) and magnetite (Fe₃O₄) minerals also form, likely from the de-carbonation of FeCO₃ → FeO → Fe₃O₄, depending on pH under the action of flow. These minerals exist across the corrosion films evidencing a more complex nature of the three-dimensional layer not currently accounted in the mechanistic models. A relatively low flow velocity (1 m/s), as recognized for industrial operations, is enough to produce chemo-mechanical damage to the FeCO₃ crystals causing breakage at low pH where dissolution of FeCO₃ occurs with a rapid crystal size reduction of the cylindrical FeCO₃ geometry of ~ 80% in just 8 hours changing also the local chemical structure of Fe₃C under the film. Similarly, flow velocity of 1 m/s is capable to induce crystal removal at neutral pH inducing further degradation of the steel compromising the protectiveness assumption of FeCO₃ corrosion films. The chemo-mechanical damage and Fe phase transformations will

affect the critical localised corrosion and therefore, they need to be accounted for in mechanistic models aiming to find new avenues for control and mitigation of carbon steel corrosion.

Keywords: pH, flow velocity, flow cell, film dissolution, mechanical damage, localized corrosion

1. Introduction

API 5L X65 grade carbon steel is one of the most common materials used for industrial pipeline construction because of the excellent mechanical properties and low cost but it is highly prone to corrosion. API 5L X65 has a typical concentration of ~98 wt.% Fe, ~0.12 wt.% C and trace amounts of other elements. Siderite (FeCO_3) and magnetite (Fe_3O_4) are the most reported corrosion products in CO_2 corrosion environments [1]; although, other phases like chukanovite ($\text{Fe}_2\text{CO}_3(\text{OH})_2$) have been also reported in laboratory studies [2, 3]. Various factors define the type of corrosion products formed on pipeline walls, e.g., temperature, pressure, flow, pH, and fluid composition [4-6]. These factors control the growth of corrosion films and determine its coverage and continuity. It has been reported that corrosion rates typically decrease when corrosion products form, and hence, it has been widely accepted that FeCO_3 corrosion films protect the steel from further degradation suggesting that the film either retards the diffusion of further corrosive species or blocks the steel surface. Models have been developed to estimate the degree of protectiveness based on the controlling factors for the growth of corrosion products and film properties (e.g., density, porosity, and thickness) but this topic is still a matter of further research [7-9].

It is known that pH influences the formation of FeCO_3 corrosion films, but it is less known what the effects are of fluids circulating at high flow velocity on the corrosion films with just few reports available [10-15]. Some of these works have reported film removal when testing flows of 4.4 m/s ($\text{Re} = 1.29 \times 10^5$) and 6.28 m/s ($\text{Re} = 1.84 \times 10^5$) using experimental setups consisting of rotating cylinders [13-15]. These works suggested that mechanical removal occurs because of wall shear stress induced by high fluid flow velocity as part of a mass-transfer process, expressed as an increase in corrosion rates. Despite these observations, the effect of flow has been diminished from an experiment using turbulent multiphase flow of up to 30 m/s [13]; however, this conclusion was reached from an experiment in absence of film, having no consideration for crystal arrangement within a fully covered corrosion film. Other

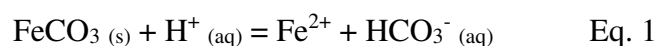
works have pointed out that intrinsic stress might be linked to film removal produced by a volume mismatch between the metal and the film [14].

In relation to chemical dissolution at low pH, it has been reported that almost total removal of the film occurs at pH 3.0 in 1 wt.% NaCl involving a mass-transfer process [15]. In addition, the combined effect of pH and flow velocity has been reported in films exposed to pH 5.8 under a flow velocity of 6.28 m/s showing partial damage of the film and yielding corrosion rates of 0.69 mm/year [16]. Similar results were obtained when 4.40 m/s flow velocity was used with a corrosion rate of 0.29 mm/year [16]. Based on these electrochemical results, it was suggested that the combined effect of pH and flow induce mechanical and chemical damage of corrosion films. Another work has explored techniques like electrochemical quartz crystal microbalance (EQCM) combined with jet impingement to evaluate kinetics of FeCO₃ dissolution under flow velocity but contrasting to the previous research, this work suggested that dissolution occurs with no mass transfer involved [17].

Undoubtedly, this information provides a good framework of the effects of two key controlling factors on the integrity of the corrosion films but still many questions remain regarding the process and the chemical changes of the films under these factors. Therefore, our work provides mechanistic insights and further understanding of the processes regarding chemical and physical changes of FeCO₃ corrosion films under the influence of pH and 1 m/s flow velocity using a multiscale and multidisciplinary approach. We combine a flow cell setup to perform the study under relevant conditions for fluid transport industries and apply molecular techniques and imaging to understand the changes incurred in the films linked to application processes.

Results and Discussion

The evaluation of the dissolution of FeCO₃ corrosion films was performed at low pH under 1 m/s flow velocity using 1% NaCl with an initial pH value of pH 3.6 which steadily increased to 4.7 during the 24 h period of the experiment (**Figure 1a**). The increase in pH indicates that H⁺ in the solution are consumed during the dissolution of FeCO₃ crystals releasing HCO₃⁻_(aq) according to equation (Eq. 1). In this reaction, the dissolution of siderite is promoted by the adsorption of H⁺ on the mineral surface which has been reported to occur between pH 2 and 5 [18].



After 24 h of the dissolution reaction, the main corrosion product identified was FeCO_3 (~97%, **Figures 1b and S1**) using siderite mineral as a reference (International Centre for Diffraction Data 8-0133) [19]; however, Fe^0 from the steel and FeO (~2%) were also quantified (**Figure 1b and S1a**).

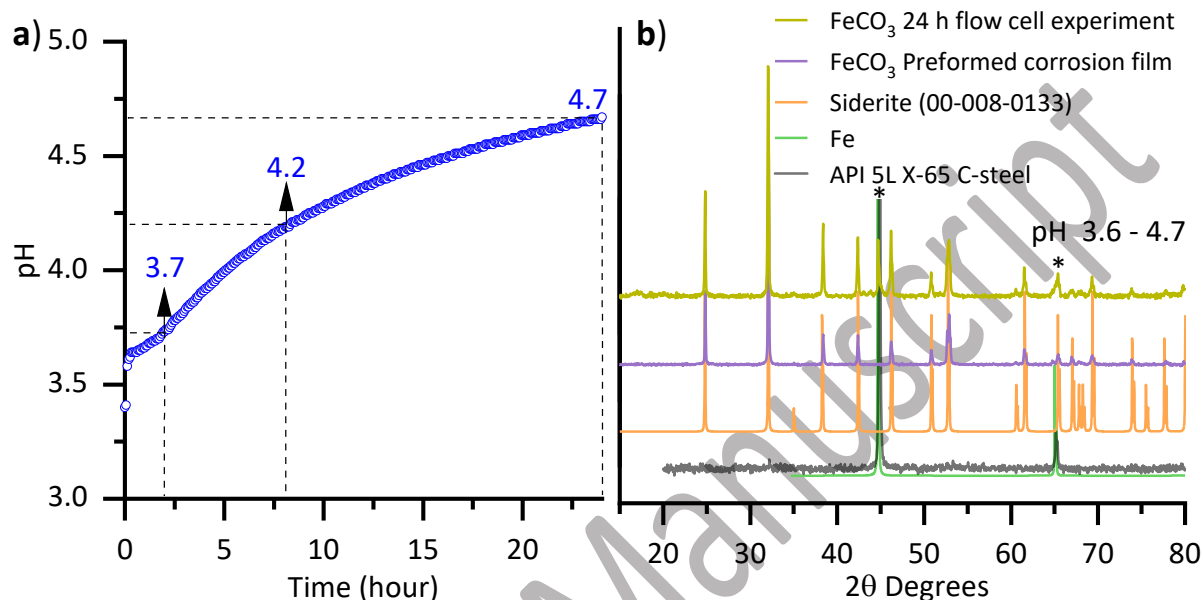


Figure 1. **a)** pH profile recorded during the dissolution experiment of the corrosion film using 1% NaCl, 80°C, 1 m/s. The pH started at 3.6 and increased to 3.7 in 2 h, then to 4.2 in 8 h, reaching a final value of 4.7 after 24 h; **b)** X-ray diffraction patterns obtained from the preformed corrosion film and from the film after dissolution experiments (pH 4.7 at the end of the experiment) at 80°C using 1% NaCl and 1m/s flow velocity. Diffraction pattern collected from API 5L X-65 C-steel as a control shows that diffraction peaks from the starting material reflect only the contribution of Fe. Most of the diffraction peaks before and after dissolution correspond to siderite (ICDD 8-0133) and those marked (*) correspond to Fe^0 from steel. For both diffraction patterns, the lack of other Fe^{3+} oxide products indicate good handling of experimental conditions to prevent air oxidation.

SEM images showed that the preformed corrosion film consisted of well-grown closely packed FeCO_3 crystals organised in random orientations with a micro-faceted cylinder and trigonal-pyramidal caps geometry as described by Ahmad et al., 2019 [20] (**Figure 2a**). The crystals were ~20-30 μm in diameter (~12 microns along the *c* axis and ~25 μm between the vertices of the planes at 120°) but they progressively downsized during the 24-hour period of the dissolution experiment (**Figs. 2b-2d and 3**). After 2 h, these crystals become slightly

rounded with rougher surfaces resulting from dissolution when the solution reached pH 3.7. Also, we observed that the number of crystals increased per area analysed ($50,000 \mu\text{m}^2$) by comparing to the number of crystals in the same area of the preformed film; this is evident in the corresponding black and white images (**Figure 2b**). We attribute this phenomenon to the rhombohedral cleavage of siderite (crystal breakage at three different planes), and it would indicate that FeCO_3 crystals experienced certain degree of mechanical damage. After 8 h, the size of the crystals further reduced to $\sim 5\text{-}10 \mu\text{m}$ in diameter becoming irregular in shape, but overall homogeneous in size (**Figure 2c**). After 8 h, the number of crystals increased ~ 2.5 times when compared to the performed film over the same area. We interpreted this as further fracture of the crystals. In addition, bare steel was visible between the remains of the highly dissolved crystals at 8 h when the pH reached 4.2; these remains still show neat surfaces without any deposited material on them (**Figure 2c**). After 24 h, some remains of FeCO_3 crystals were visible on the surface of the steel; however, new re-precipitated material, that was not present in the first 8 h, was evidently filling the gaps between the crystal remains covering again the bare steel. This suggests that FeCO_3 re-precipitated during the increase of pH from 4.2 to 4.7. These observations indicate that dissolution and re-precipitation processes would modify the thickness and the porosity of the film over time.

We hypothesize that if re-precipitation of FeCO_3 occurred, the process would involve the reaction of Fe^{2+} in the brine, which has been enriched from the previous dissolution of FeCO_3 . This dissolution process also releases HCO_3^- reflected by the increase of pH in the brine solution. FeCO_3 crystal remains, acting as seeds, will provide surface nucleation sites that altogether with local favorable saturation conditions promoted by higher pH values than in the bulk solution, and higher concentrations of HCO_3^- and CO_3^{2-} would support re-precipitation of FeCO_3 .

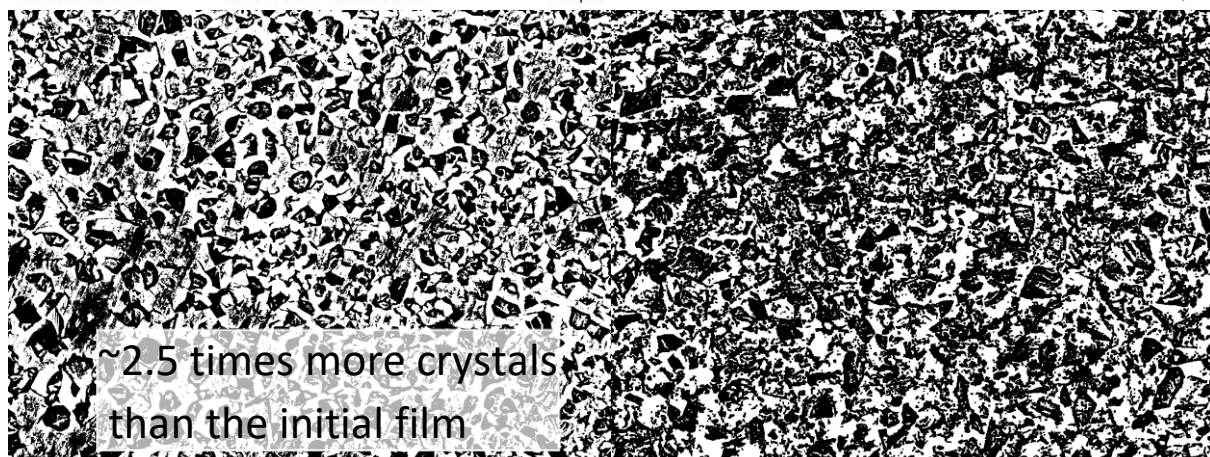
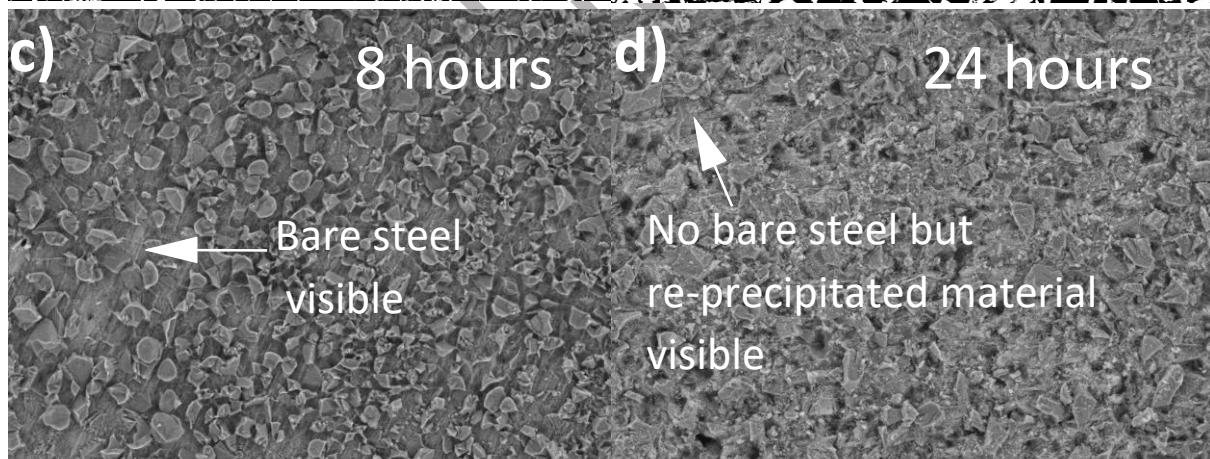
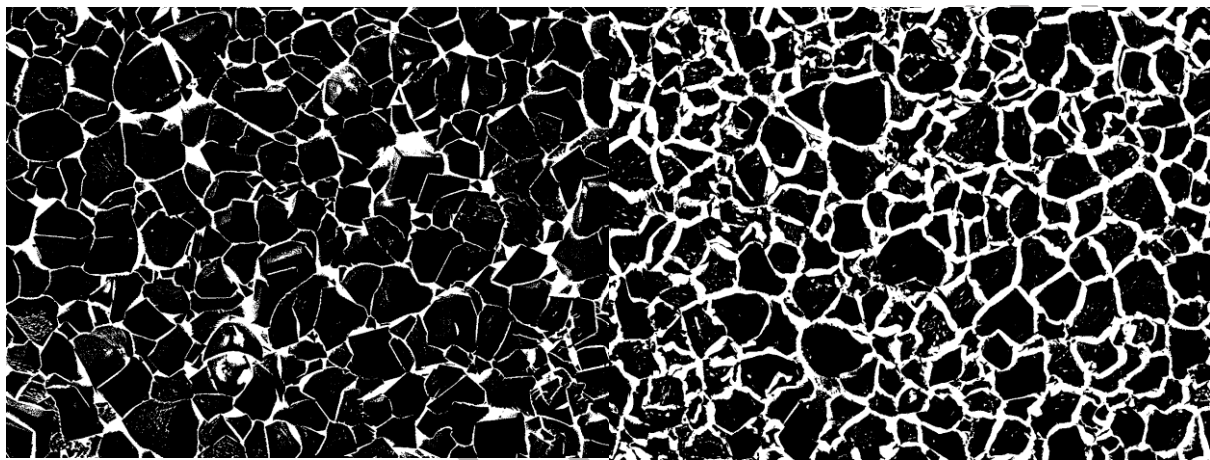
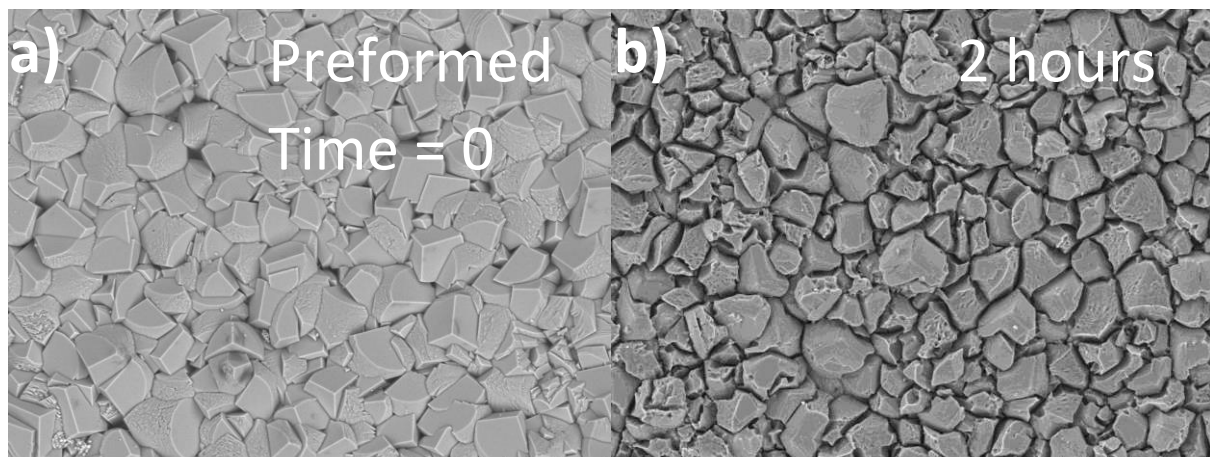


Figure 2. SEM images of FeCO_3 corrosion films and the corresponding black and white (B&W) binary images. **a)** Preformed film as initially observed at the beginning of flow experiments (time = 0, initial pH 3.6); **b)** corrosion film after 2 h of dissolution using 1% NaCl and 1 m/s flow velocity at 80°C. Signs of crystal dissolution and size reduction were evident from the wider gaps observed between the crystals in the corresponding B&W image. Furthermore, the number of crystals increased in the image field view suggesting breakage of the initial crystals (time=0); **c)** corrosion film after 8 h under the same conditions as in (b) showing further reduction in size and uncovering the steel; the number of crystals increased by ~2.5 times compared to the preformed film (time = 0); **d)** corrosion film after 24 h at the same conditions as in (b) but the bare steel is not visible anymore and instead fresh precipitation is observed, which occurred between 8 h and 24 h. Cross-sectional view images of all corrosion films here presented are shown in **Figure S2**.

Quantification of the size reduction and number of crystals are presented in **Figure 3**. The distribution of the crystal size over 50,000 μm^2 of the specimen is presented in **Figure 3a**. The preformed film had larger crystal size distribution than films exposed to dissolution experiments. It is worth to note that specimens used for dissolution (i.e., 2 h, 8 h and 24 h) were all from the same growth batch ensuring the same characteristics of crystal size and surface coverage. Figure **3a** shows that 50% of the crystals from the preformed film had areas between ~60 and ~260 μm^2 with a median value of ~140 μm^2 ; however, the presence of larger crystals (the top 25 percentile) increases the mean value to 442 μm^2 . After 2 h dissolution, the crystal size reduced by ~50% (~60 and ~180 μm^2) with a median value of 106 μm^2 , yielding a homogeneous distribution. This means that within 2 h, the crystals reduced 25% from their original size using the median value as reference. After 8 h, the size reduction was ~80% and the number of crystals increased by about 2.5 times (**Figure 3b** boxplots). These results quantify the significant chemical and mechanical damage of the film caused by low pH in flow conditions.

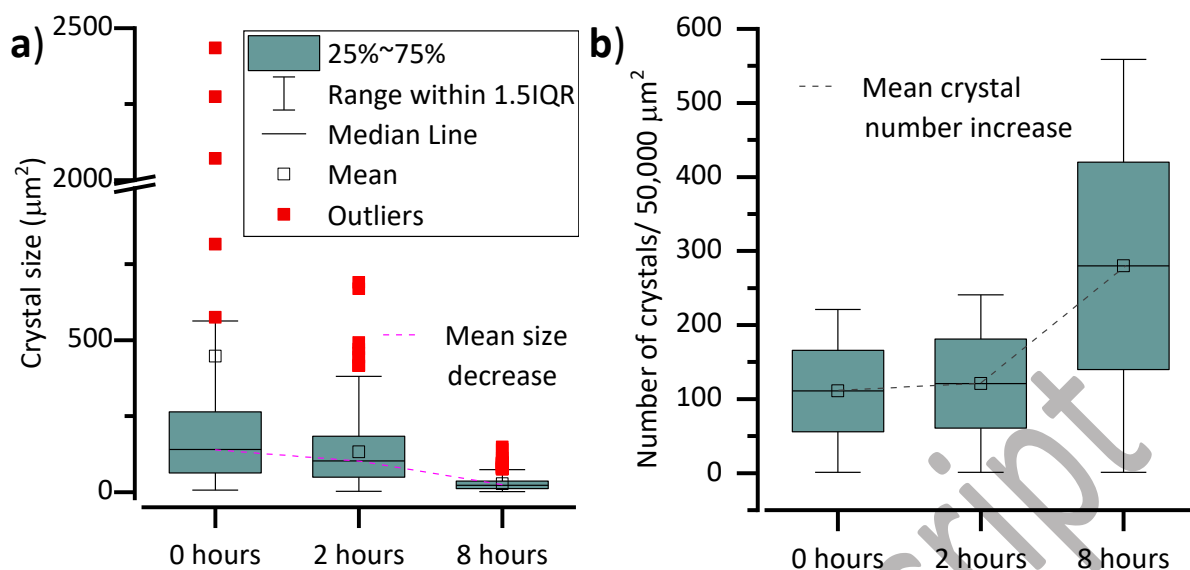


Figure 3. **a)** FeCO_3 crystal size (μm^2) distribution quantified over 50,000 μm^2 of the preformed film (time =0) and over the same area of films after 2 h and 8 h of dissolution experiments; **b)** distribution of the number of crystals over the same areas and films as in (a).

Surface chemical characterization (top 10 nm) of the preformed film revealed siderite (FeCO_3) as the main corrosion product (57%); however, a large proportion (35%) consisted of magnetite (Fe_3O_4) and to a lesser extent (8%) wustite (FeO) (**Figure 4a** and **Table S1**). After exposing the specimens to 1 m/s flow at 80°C for 8 h when the solution reached pH 4.2, the film surface was mainly composed of FeCO_3 (92%) and FeO (8%) (**Figure 4b**). At the end of the 24 period, the film was mainly FeCO_3 (88%) and Fe^0 (12%) (**Figure 4c**). These results indicate that on the surface, FeO and Fe_3O_4 also formed during the growth of FeCO_3 (at pH ~7 and 80°C) but they dissolved from the surface during the dissolution experiments at low pH, first Fe_3O_4 then FeO . These two minerals likely formed as by-products of FeCO_3 from the de-carbonation of FeCO_3 , a process that increases the O_2 fugacity in the system as reported to occur in a small although stable field in the $\text{Fe-CO}_2\text{-H}_2\text{O}$ system [21, 22]. Furthermore, FeO likely formed first and then transformed to Fe_3O_4 at pH near neutral and high temperature (at and above 80°C) as previously reported [21, 23-25].

Changes in the chemistry of the corrosion products are highly dependent on pH; thus, the amount and type of Fe species in corrosion films will describe the variability in the conditions during industrial operations. Various Fe oxide species have been reported in oil and gas operations under CO_2 environments [21, 26, 27]. In this work, the surface of the preformed corrosion film (grown at pH 7.0 and 80°C) contained mainly FeCO_3 and minor

amounts of FeO and Fe₃O₄. Dissolution of Fe₃O₄ occurred from the surface as soon as the specimen was exposed to low pH releasing Fe²⁺ to the solution via congruent reduction and therefore, it was not present after dissolution at this condition [28, 29]. As mentioned above, FeO likely resulted from the decomposition of FeCO₃ (into FeO and CO₂) which has been demonstrated to occur at temperatures below 100°C [30]. In addition, FeO is often described as an intermediate product towards the transformation to Fe₃O₄ in CO₂ environments; and therefore, it is likely that the order of formation of these corrosion products has been FeCO₃ → FeO → Fe₃O₄. It is worth noting that if oxygen is present, FeO rapidly transforms to Fe₂O₃ [30-32].

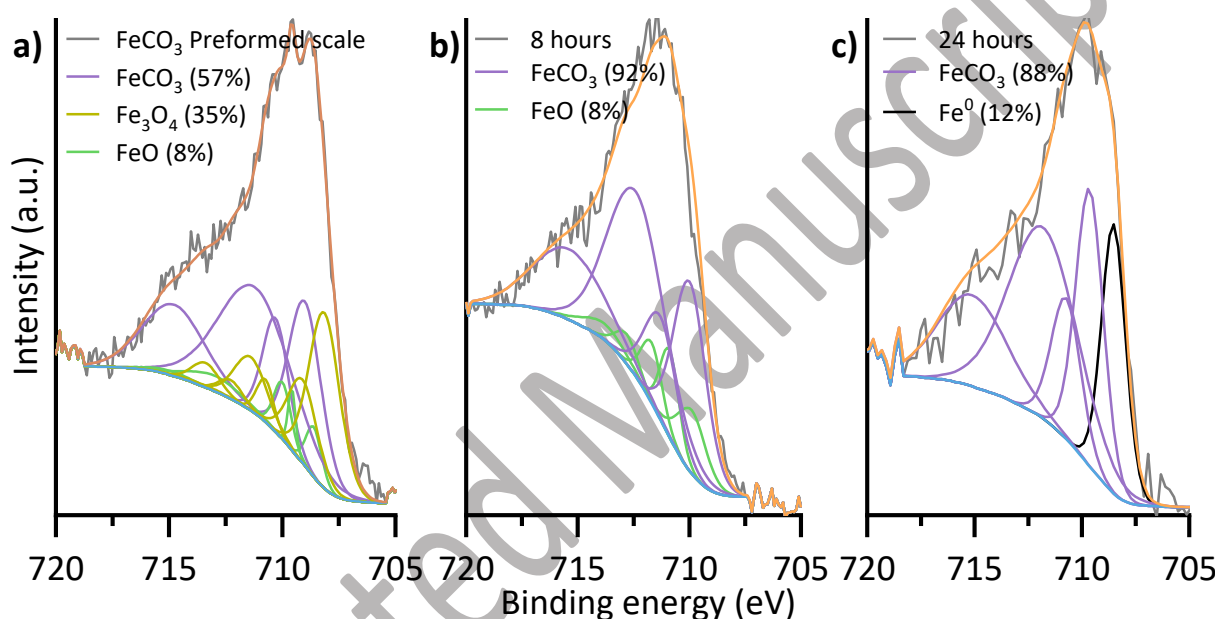


Figure 4. Fe 2p_{3/2} XPS spectra collected from the surface of **a)** preformed corrosion product film grown at pH 7.0; **b)** and **c)** specimens under 1 m/s flow, 80°C and pH between 3.6 (at the start) and 4.7 (after 24 h).

The chemical composition of the preformed corrosion film was confirmed through μ -XANES mapping characterisation (**Figure 5**). The optical microscopy image of the cross-section analysed from the preformed corrosion film is presented in **Figure 5a**. The corresponding XANES map shows three clusters that represent three different local chemical environments of Fe in the cross section of the film (**Figs. 5b and 5c**). Fe K-edge XANES spectra typically are characterized by a pre-edge (first peak) and the edge (main peak) which both provide information about the oxidation state and site symmetry of the absorbing atom (e.g., **Figure 5d**). The pre-edge peak is due to the dipole-forbidden $1s \rightarrow 3d$ transition and is sensitive to spin state, oxidation state and other elements surrounding the absorbing atom. It is only observed in the presence of a $3d \rightarrow 4p$ orbital mixing or direct quadrupolar coupling. On the other hand, the edge is caused by the transition $1s \rightarrow 4p$, and because the outer p-orbitals are more sensitive to electronic changes, the average valence state of the absorbing atom can be estimated from the position of the main absorption edge (main peak) with respect to standards [33]. As the valence state of the central absorbing atom decreases, all the main features shift to lower energies and vice versa. Spectrum I of the preformed corrosion film showed a pre-edge and edge close to that of FeCO_3 standard (**Figure 5d**). Cementite (Fe_3C) and Fe^0 were both identified in spectrum III; however, changes in the local environment of cementite were identified with an increase in the pre-edge intensity with respect to the Fe_3C standard (**Figure 6c**).

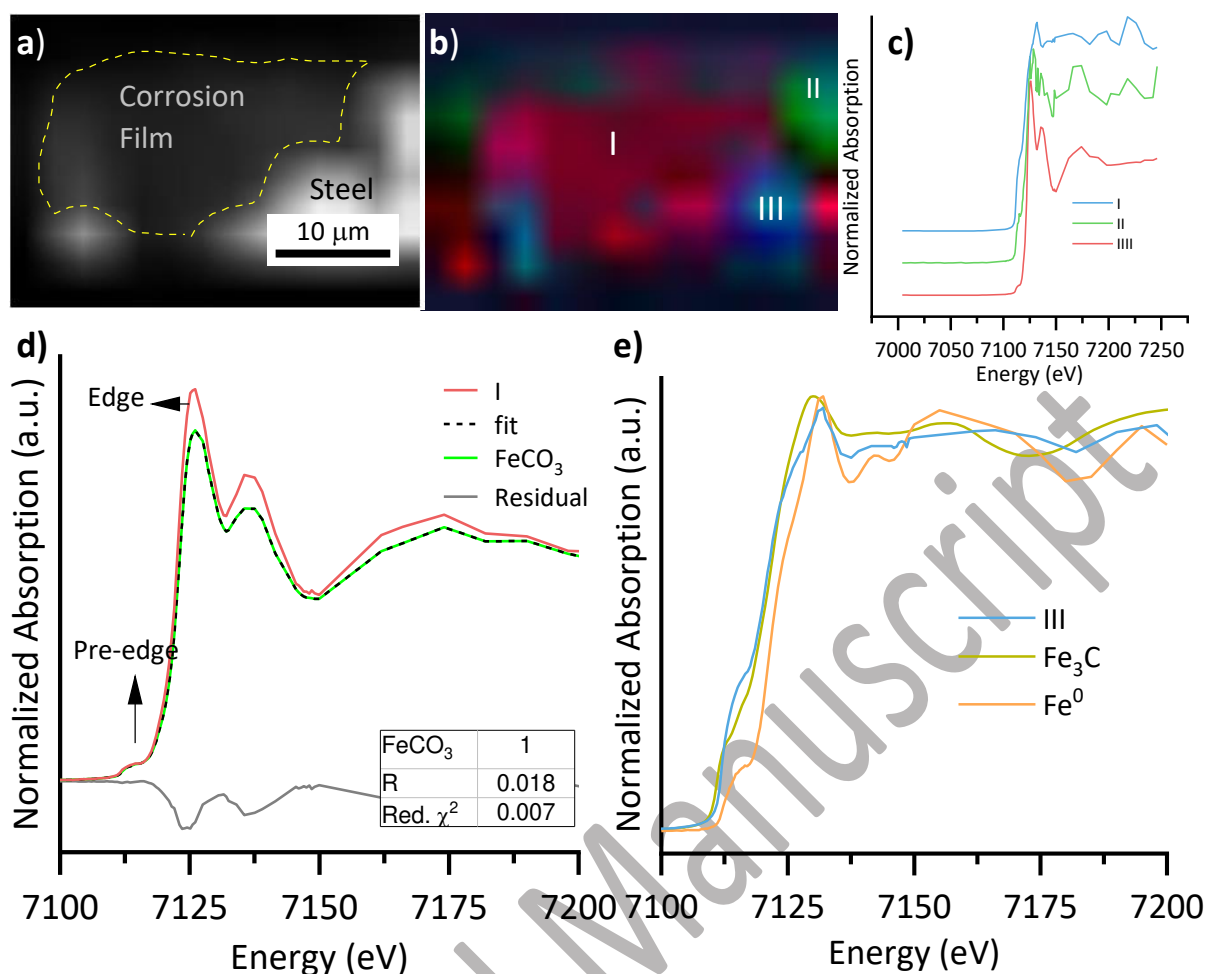


Figure 5. **a)** Optical microscope image of the cross section lamella containing the corrosion film (marked area) and steel (area in white) at pH 7.0 and 80°C; **b)** XANES cluster map (43 μm x 44 μm); **c)** Fe K-edge XANES spectra I, II and III of cluster regions identified on the map; **d)** Fe k-edge XANES spectrum I and LCF (full energy range collected is shown in **Figure S3**); **e)** Fe K-edge XANES spectrum III compared to Fe⁰ and Fe₃C spectra.

Figures 6a and 6b show the optical microscopy image and XANES map from the corrosion film after 24-hour dissolution at low pH. It is worth to mention that corrosion products after the 24-hour dissolution experiment were scarce as most of the film has already dissolved; therefore, information extracted from the film at these conditions is limited. Nevertheless, three clusters were identified on the cross-section of the specimen (**Figure 6b**). All spectra consisted of combinations of Fe₃C and Fe⁰ quantified by LCF; however, the fingerprints are slightly different on the pre-edge feature suggesting changes in the local environment of Fe, particularly on regions close to the steel where the pre-edge showed an intensity increase (**Figs. 6c and 6d**) [34]. This indicates that not only the film is chemically changing but also

the material under the film (e.g., Fe_3C). Spectrum I was quantified to contain a mixture of Fe_3C (30%) in line with the cementite standard and Fe^0 (70%). Spectrum II showed the highest amount of Fe_3C (93%), while spectrum III was richer in Fe^0 (95%). The pre-edge of spectra II and III showed changes in the intensity and shape of the peak, shifting towards lower energy values with respect to both Fe^0 and Fe_3C standards. This intensity change represents average electronic changes in the transitions $1s\ 3d$ of both phases suggesting wider distribution of orbitals that possibly are because of the breaking of the crystalline long-range order of Fe_3C and Fe^0 phases [35]. It could be also possible that the smothering of the pre-edge relates to the formation of $\text{Fe-Fe}_3\text{C}$ as reported to occur [34]. These results evidence the simultaneous changes on the Fe_3C structure under the film which contributes to degradation of the steel as the corrosion film dissolves.

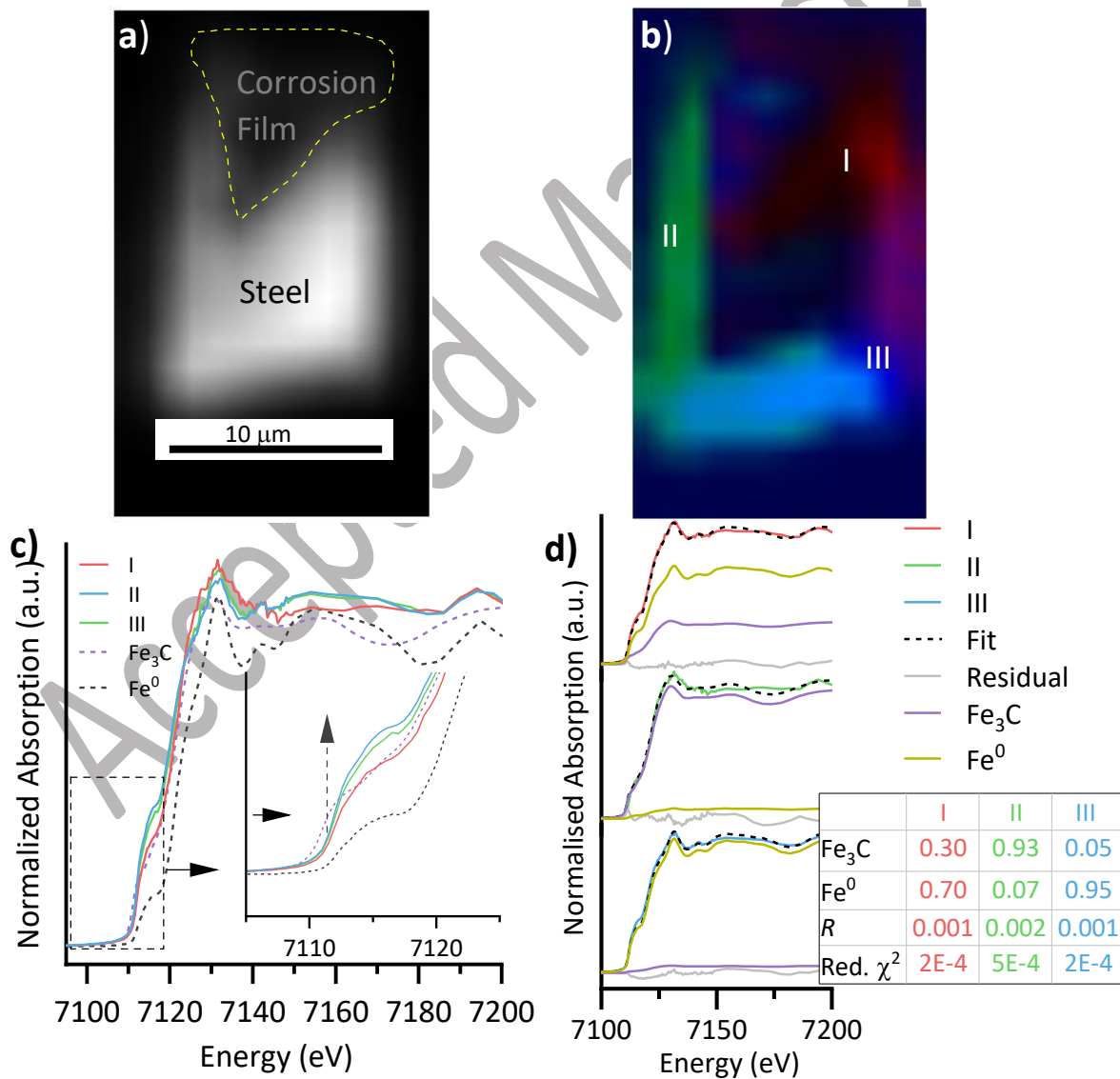


Figure 6. **a)** Optical microscope image of the cross section containing the corrosion film (marked area) and steel (area in white) after dissolution experiment at pH 3.6, 80°C using 1% NaCl and 1m/s flow velocity; **b)** XANES cluster map (16 μm x 30 μm) identifying three slightly different Fe local environments; **c)** Fe K-edge XANES spectra I, II and III showing differences in pre-edge intensities and energy shift (full energy range presented in **Figure S4**); **d)** Fe k-edge XANES spectra I, II and III and LCF (full energy range of these spectra are shown in **Figure S5**).

FeCO_3 corrosion films under flow at neutral pH perform different than those at low pH as shown in figure 7. Our observations indicated that entire crystals were removed from the FeCO_3 film shortly after the experiments started. After 2 h, gaps between the crystals were visible, and the frequency of those gaps increased over the 8 h and 24 h tests. The fact that these gaps were inexistent at the beginning of the experiment indicate that they were induced by mechanical damage as crystal fragments seen inside these gaps support this hypothesis (**Figure 7c** and **7d**). We interpret this phenomenon as induced localized corrosion because dissolution of FeCO_3 at neutral pH is not a favourable process. Dissolution under the film is neither a prevalent process at pH 7.0 but possibly the porous material frequently observed under the FeCO_3 crystals can itself contribute as a weak point of attachment of the crystals to the steel decreasing the shear stress required to remove the crystals from the film. Another explanation that could support crystal removal is a mechanical effect under the inverse pseudo Hall-Petch relation that can be explained by the weakest-link model which describes failure behaviour of brittle materials [36].

As mentioned before, it has been suggested that removal of corrosion films by the action of high flow velocities (up to 30 m/s) is unlikely [13] but this suggestion was made from a system without the presence of corrosion film dismissing the structure and crystal arrangement of corrosion products that conform the film. In contradiction, corrosion film removal was reported when exposed to fluids under lower flow velocities (i.e., 4.4 m/s and 6.28 m/s) [15]. In this work, the preformed film consisted of relatively large well-packed crystals randomly oriented with sliding boundaries (**Figure 7a**). Being FeCO_3 a brittle material, its failure depends on number and distribution of structural defects as described by the weakest-link model (linked to the inverse Hall-Petch relation), which has been successfully applied to study the failure of brittle materials such as graphene and perovskites. In this model, grain boundary junctions (weak-links defects) are considered the weakest points for failure. The number and distribution of boundary junctions are highly affected by

crystal arrangements in different orientations, which have different atomic structures and boundary energies; and therefore, different failure strengths. In other words, different configurations of grain boundaries will yield different configurations and large distribution of grain boundary junctions that contribute to the failure of the material [36, 37]. Therefore, the polycrystalline FeCO_3 crystals conforming the preformed corrosion film should contain a large number and distribution of boundary junctions that can be considered as weak-links within the model. This can initiate nucleation cracks expressed themselves as entire crystal removal from the corrosion film under the flow conditions used. Overall, the mechanical damage of the corrosion film at neutral pH indicates that even if the conditions are favourable for FeCO_3 formation it does not mean that the film protects the steel, and the demonstrated damage of an existent corrosion film promotes the contact of the material underneath to corrosive species in the brine solution.

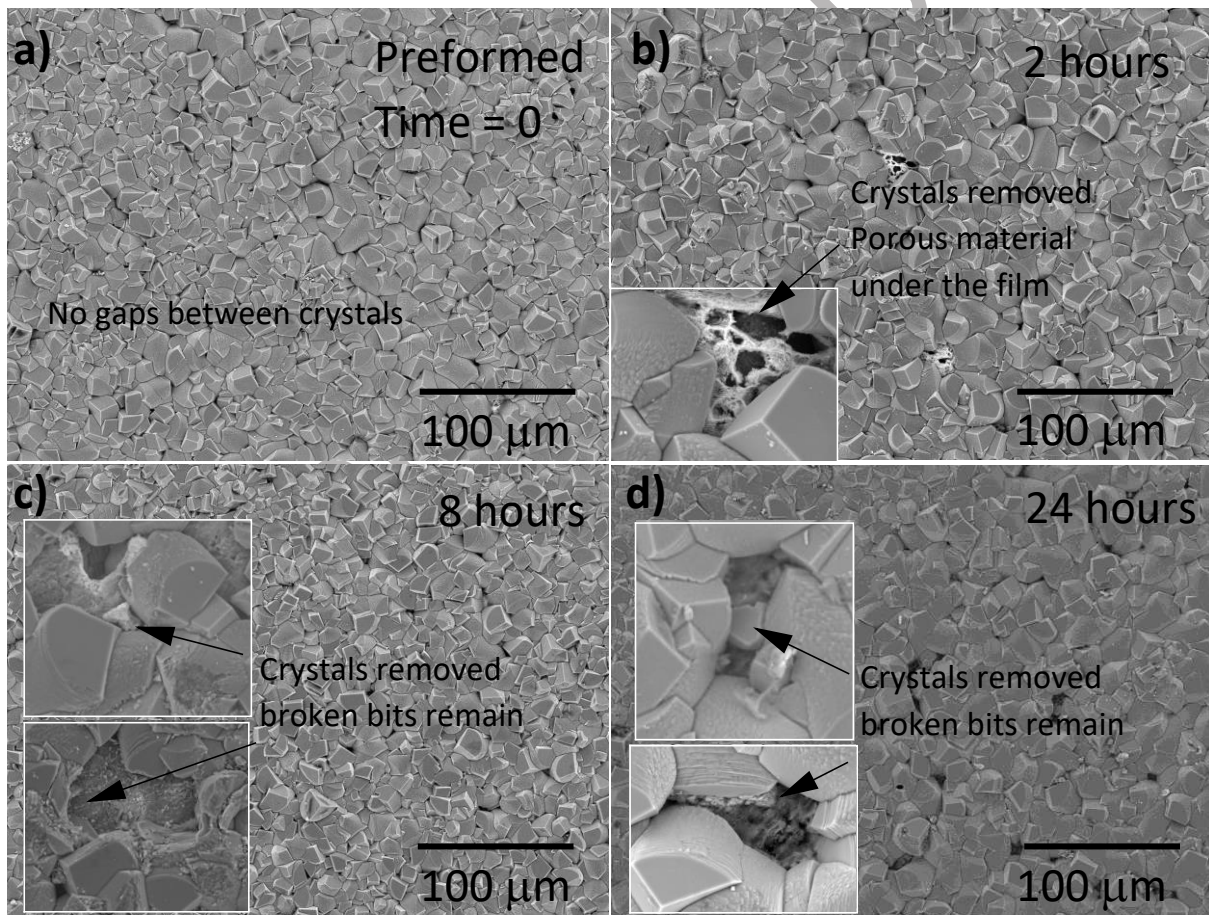


Figure 7. SEM images of **a)** the preformed FeCO_3 film used in flow experiments for 2 h, 8 h and 24 h. The preformed film was grown at 80°C using 1% NaCl adjusted to pH 7.0 using NaHCO_3 and with a total pressure of 30 bar for 72 h. Specimens from the same growth batch were used in all flow experiments; **b-d)** FeCO_3 films after 2 h, 8 h and 24 h of flow

experiments. As observed, the preformed film had full coverage with no gaps between the crystals but after flow experiments, all films showed entire crystals missing from the film that progressively increased in frequency over time; phenomenon that we interpreted as localised corrosion ($\sim 50\mu\text{m} \times 15\mu\text{m}$).

As expected, diffraction data showed FeCO_3 as the main corrosion product before and after flow experiments at pH 7.0 because no dissolution of the corrosion products occurred (**Figure 8a**). Chemical information from the film surface, evidenced the presence of magnetite ($\sim 50\%$) that as mentioned above can form either directly from precipitation of $\text{Fe}^{2+}_{(\text{aq})}$ or from the transformation of FeCO_3 , directly or via FeO depending on f_{O_2} (**Figure 8b** and **Table S2**). The presence of magnetite and FeO across the film at pH 7.0 was also confirmed by μ -XANES. The optical microscopy image from the cross-section and μ -XANES map are shown in **figure 9a**. Three clusters were identified on the cross section of the specimen at these conditions that indicated the presence of FeCO_3 , Fe_3O_4 and FeO . Spectrum I representative from the bulk of the film was mainly composed of FeCO_3 (100%) (**Figure 9d**). Spectrum II showed a more reactive region with 74% FeCO_3 , 12% FeO and 14% Fe_3O_4 and indicating that a significant transformation from siderite to Fe oxides occurred, possibly aided by the action of temperature and flow (**Figure 9e**). Interestingly, the areas with corrosion products close to the steel (spectrum III) showed the highest proportion of Fe oxides with 24% FeO and 18% Fe_3O_4 , and 58% corresponded to FeCO_3 (**Figure 9f**).

These results evidence that Fe_3O_4 consistently forms at pH 7 as a corrosion product yet the amount is small as the conditions are still favourable to form FeCO_3 . Given their stabilities, the most likely phases to be observed as corrosion products in operational pipelines under the conditions tested would be FeCO_3 , Fe_3O_4 and Fe_2O_3 . This is valid if other cations are not present. That means packing different type of corrosion products with different morphologies will change the film, and this will have direct effects on porosity and permeability.

Furthermore, different Fe phases as corrosion products will have different reactivities will differ depending on environment conditions. We can hypothesise that the transformation of FeCO_3 to Fe_3O_4 could occur by an increase in the f_{O_2} . Oxygen can be supplied by either the gas phase, dissolved in the fluid, a mineral (e.g., FeO) or even by CO_2 itself. That would define different reactions depending on the source of oxygen and concentration, but from a general equation the reaction could be $3\text{FeCO}_3 + \frac{1}{2} \text{O}_2 = \text{Fe}_3\text{O}_4 + 3\text{CO}_2^{2-}$. However, another pathway of transformation could also occur via FeO by further oxidation of FeO , $3\text{FeO} + \frac{1}{2} \text{O}_2 = \text{Fe}_3\text{O}_4$.

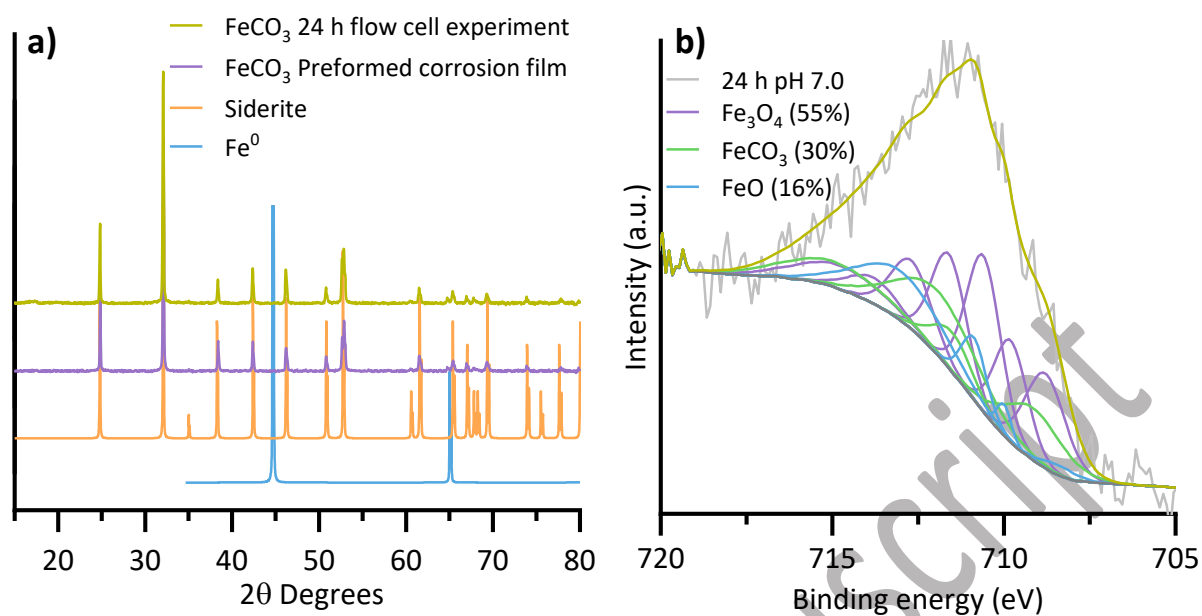


Figure 8. a) Diffraction patterns of the preformed corrosion film and of the film after flow experiment at pH 7.0 compared to Fe and siderite references; b) XPS data of the film after 24 h flow experiment.

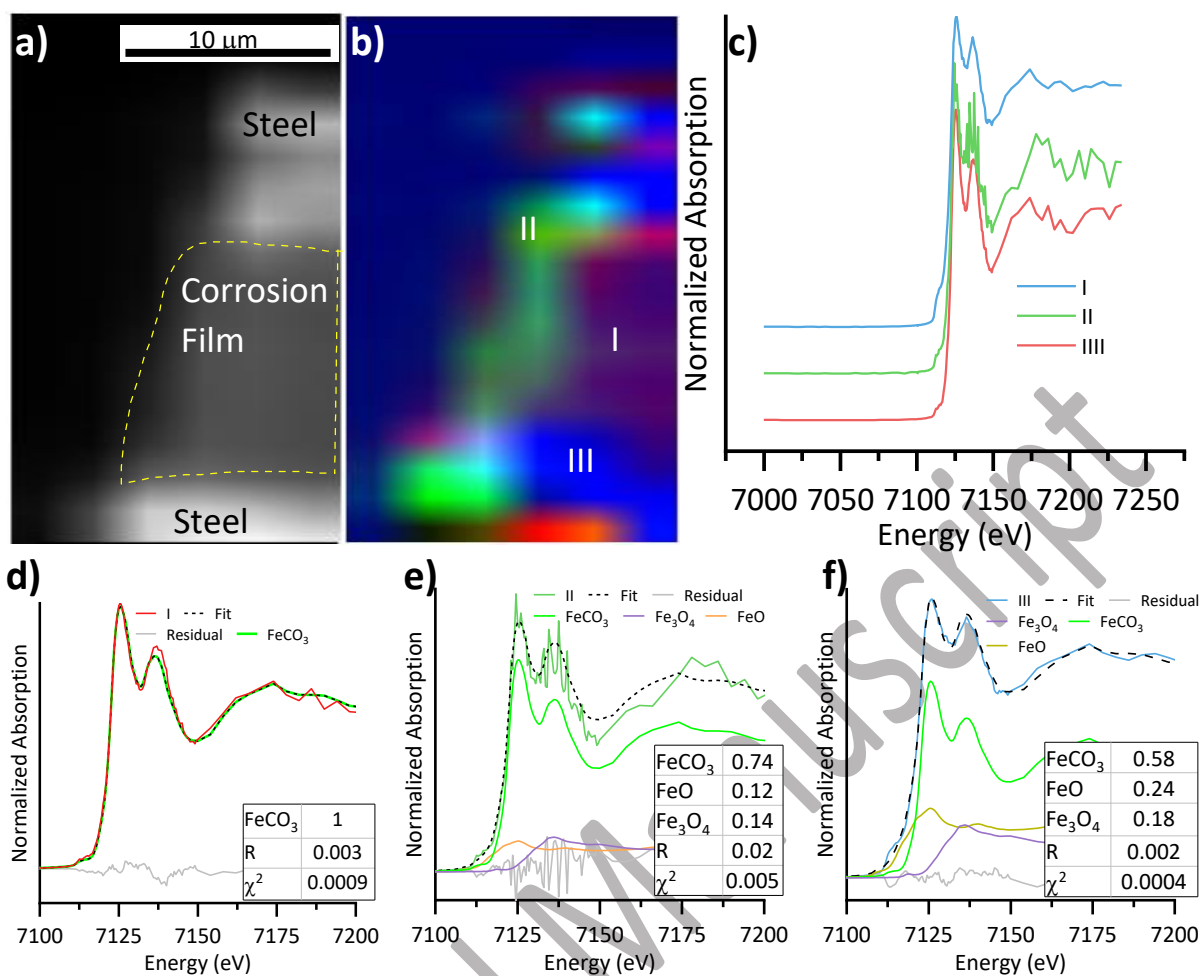


Figure 9. **a)** Optical microscope image of the cross section containing the corrosion film after 24 h flow experiment and steel (pH 7.0, 80°C, 1m/s flow velocity); **b)** XANES cluster map (16 µm x 30 µm); **c)** Fe K-edge XANES spectra I, II and III; **d-f)** Fe k-edge XANES spectrum I, II and III and LCF (full range of energy presented in **figures S6-S8**).

Chemical dissolution of FeCO_3 crystals was demonstrated to be a pH-driven process. Starting at pH 3.6, H^+ from the solution react with FeCO_3 crystals from the film with the release of Fe^{2+} and HCO_3^- ions increasing the pH of the solution. Simultaneous dissociation of FeCO_3 in solution ($\text{Fe}^{2+} + \text{CO}_3^{2-} + \text{H}_2\text{O}$) of the crystals yields to the production of OH^- and HCO_3^- ions, also increasing the pH of the solution. The chemical dissolution is significantly aided by the flow causing crystal breakage in up to 80% in a short period of time (8 h) producing also changes in the material under the corrosion film. Contrary at pH 7.0, crystal removal was the most notorious physical change in the film promoting direct contact of the fluid to the material under the film. The transformation of FeCO_3 to FeO at 80°C aided by flow suggest another pathway of formation of FeO as corrosion product; however, it can be either transformed to Fe_3O_4 in CO_2 environments or rapidly transformed to Fe_2O_3 in presence of O_2 .

Conclusions

Wustite (FeO) and magnetite (Fe_3O_4) are confirmed corrosion products to form along with siderite (FeCO_3) at neutral pH, 80°C in CO_2 environments; however, FeCO_3 is the dominant and more stable product under these conditions. The formation of FeO and Fe_3O_4 can also occur through the transformation of FeCO_3 depending on pH conditions and likely the action of flow. The transformation follows the sequence, FeCO_3 , FeO and Fe_3O_4 in CO_2 environments confirmed to exist in the three-dimensional corrosion layer. Chemical changes are not limited to the film but to the material underneath with changes confirmed at the molecular level in Fe_3C which contributes to the degradation of steel. This has serious implications in industrial operations as the use of low pH fluids in the cleaning process of pipelines not only dissolve the corrosion products but also the steel. At the lower end of demanding CO_2 environments, under conditions that induce FeCO_3 dissolution, the reduction of crystal size of the cylindrical FeCO_3 geometry is so rapid that in 8 h crystals are ~80% smaller but homogeneous in size. The action of flow cause crystal breakage contributing to the breakdown of the corrosion films at both low and neutral pH, being a key factor indirectly contributing to the further degradation of steel; however, flow in combination with pH accelerate damage of the film. The influence of pH on the nature of corrosion products and the combined effect of mechanical damage and time will define the quality of the film; however, systems under flow compromise the protective assumption of FeCO_3 corrosion films. Changing operation conditions will define different crystal morphologies, and therefore different packing and subsequent changes in the mechanical properties that define how the film react those conditions. The chemo-mechanical damage and Fe phase

transformations will affect the critical localised corrosion and therefore, they need to be accounted for in mechanistic models aiming to find new avenues for control and mitigation of carbon steel corrosion.

Methods

In this study, FeCO_3 corrosion films were grown in an autoclave reactor and then used in flow-cell experiments in conditions detailed below (**Figure S9**). Fast-rinse and air-dried specimens were transferred immediately from the autoclave to a desiccator which was maintained under vacuum. Specimens were only removed from the desiccator for immediate use in flow experiments or for characterisation analysis. The drying and transfer procedures were always completed in less than 2 minutes to avoid air oxidation or contamination. Fresh prepared specimens were used in flow experiments and characterisation analyses. Transfer of specimens to the instruments for characterization was performed in vacuum sealed bags. We used API 5L X65 C-steel as a testing material with a ferritic-pearlitic microstructure with an specified elemental composition (wt. %) consisting of Fe (97.8), C (0.12), Si (0.18), Mn (1.27), P (0.008), S(0.002), Cr (0.11), Mo (0.17), Ni (0.07), Cu (0.12), Sn (0.008), Al (0.022), B (0.0005), Nb (0.054), Ti (0.001) and V (0.057). Cylindrical X65 C-steel specimens of 10 mm in diameter and 6.25 mm in thickness with a total surface area of $\sim 5.49 \text{ cm}^2$ were manufactured. A hole was tapped in the centre of the base for mounting onto a custom-made holder inside the autoclave reactor. Prior film growth, C-steel specimens were wet-ground using progressively 120, 320 and 600 silicon carbide (SiC) grit papers. They were then rinsed with DI water, acetone and then dried with air. For the solutions, we used NaCl (Fluka/Honeywell CAS 7647-14-5 99%) and NaHCO_3 (Alfa Aesar 99% CAS 144-55-8).

Corrosion film growth was performed using five C-steel specimens per experiment that were attached onto the holder and fixed to the shaft of the autoclave lid (**Figure S1b**). An unstirred 1% NaCl solution saturated with CO_2 for 24 h was placed in the autoclave and the pH was adjusted to 7.0 at 80°C using NaHCO_3 . FeCO_3 corrosion films were grown in static mode at 80°C under a CO_2 total pressure of 30 bar for 72 h. The surface area of the specimen to solution volume ratio (A/V) was kept to $\sim 42 \text{ cm}^2/\text{L}$.

The specimens with preformed FeCO_3 corrosion films (from the autoclave) were used in the flow experiments (1% NaCl circulating with a flow velocity of 1 m/s at 80°C , $0.54 p_{\text{CO}_2}$ bar) at pH 3.6, to test for dissolution, and at pH 7.0 to evaluate mechanical damage (while preventing dissolution) (**Figure S1c**). Both types of experiments were performed at identical

saturation degree conditions. The pH of the brine solutions was adjusted at the beginning, NaHCO_3 was used to adjust the pH to 7.0. The pH was constantly monitored throughout the reaction. Experiments were performed in duplicates at each of the three times of reaction evaluated (i.e., 2 h, 8 h and 24 h) and the two pH conditions evaluated. The experimental setup consisted of a closed loop that transported the solution between a glass reactor and a custom-built flow-cell described and validated to work with a flow of 1 m/s, which was quantified to be a turbulent flow (Reynolds number of 16445) with a shear stress of 3.15 Pa. Details of the design of the flow cell shown in **figure S1c** can be found in Burkle et al., 2016 [38]. The flow was controlled through a customised high precision magnetic drive gear micro-pump (Micropump® Series GJ-N25). The reactor consisted of a glass reaction vessel with a lid fitted with a pH electrode, inlet and outlet for gas and solution, and a condenser. The custom-made flow-cell comprised two main components, a base and a windowed top secured together with screws. The base of the cell contained a compartment where the C-steel specimen was placed.

To perform the experiments, 1L of 1% NaCl solution was stirred and flushed with CO_2 for 24 h while attached to the closed loop of the flow-cell rig. The solution was heated up to 80°C and the pH was adjusted to either 3.6 or 7.0 with NaHCO_3 , if necessary. Once the solution reached the temperature and pH values, the specimen with the preformed corrosion film was placed at the base of the flow-cell and the full setup was left to deaerate for further 15 minutes. The dissolved oxygen concentration was then confirmed to be below 50 ppb using a DO probe (Intellical™ LDO101) before starting the experiment and then the solution was circulated through the closed loop. The pH was recorded automatically over the length of the experiment using a pH and conductivity meter (Mettler Toledo S213). Three experiments were performed at pH 3.6 for 2, 8 and 24 h, and three experiments at pH 7.0 for the same time duration.

For specimen characterization, we used a complementary approach of analysis at different dimension scales. X-ray diffraction (XRD) and scanning electron microscopy (SEM) were used to collect information from the corrosion products. X-ray Photoelectron spectroscopy (XPS) was used to analyse the chemical composition at the surface of the FeCO_3 film up to 10 nm. Micro X-ray absorption near edge spectroscopy (μ -XANES) was used to investigate speciation of Fe products of cross-sections of the FeCO_3 films at the micron level.

After completion of flow experiments, the specimens were rapidly removed from the flow-cell, rinsed with DI water, dried immediately with air, and then stored in a vacuum desiccator while they were transferred to the instruments. This process was always completed in less than 2 minutes. XRD and SEM were used to investigate the composition and morphology of the corrosion products. For XRD analysis, the cylindrical specimens were mounted onto a holder and scanned from 15 to 80° 2 θ at 1.55°/min using a Bruker D8 X-ray diffractometer. The diffraction patterns were compared against the diffraction data of the structure of siderite and α -Fe [19, 39]. For SEM imaging acquisition, a TM3030Plus microscope was used. The specimens were fixed onto stubs using high purity double-sided conductive adhesive carbon tabs and mounted on the sample stage of the instrument which was operated at 15kV. To aid the analysis, areas of 250 μ m x 200 μ m over the images were converted to black and white binary images to quantify number of crystals and size of the preformed film (time =0) and films after flow experiments at 2 h, 8 h and 24 h. This was performed on at least three different areas of each specimen. All the images were analysed using the ImageJ software [40].

XPS data were collected using an EnviroESCA system equipped with a monochromatic Al K α (1.487 keV) X-ray source. The instrument was operated at 3.3 mbar and ⁴⁸Ar gas was used for charge compensation. Specimens were fixed onto stubs using high purity double-sided conductive adhesive carbon tabs. The area analysed was 300 μ m x 300 μ m. Survey spectra were collected between 15 and 1500 eV with a pass energy of 100 eV. High-resolution spectra were collected at the binding energies of Fe (700–740 eV), O (525–545 eV) and C (280–295 eV), with a pass energy of 20 eV and a step size of 0.1 eV. Calibration of the binding energies was performed using the carbon 1 s peak at 285 eV using CasaXPS software [41]. Fe 2p_{3/2} high-resolution spectra were fitted using multiple peaks and Shirley background subtraction.

μ -XANES mapping was performed on beamline I18 at Diamond Light Source. The measurements were performed using a cryogenically cooled Si (111) monochromator and two Rh-coated Si mirrors for horizontal and vertical X-ray beam focusing using a Kirkpatrick-Baez (KB) configuration.

Samples were prepared as FIB lamellae across the steel and corrosion film using a Focused Ion Beam FEI Helios G4 CX Dual Beam microscope. Prior FIB preparation, the specimens were embedded in resin and the cross section was exposed through fast polishing using 600

SiC grit paper; the cross section was immediately dried with air. The specimens were coated with Ir (20 μm) using an Agar Scientific sputter coater to minimise charge effects. An additional Pt protection layer (20 μm length x by 2 μm width and 1 μm thick) was applied in-situ using a Ga^+ Ion beam. Material was removed from either side of the lamella using 21 nA and thinned using 9 nA. The lamella was Pt welded to an easy-lift needle, released from the bulk then re-attached to a TEM FIB grid. Then, the lamella was thinned using progressively smaller beam current (0.79 nA – 40 pA) until a thickness between 500- 1000 nm was achieved.

For the μ -XANES mapping, the FIB lamellae were placed at 45° to the incident beam and the energy-dispersive silicon drift 4-element Vortex ME-4 detector with Cube pre-amplifier was positioned normal to the beam direction. The monochromator was calibrated using an Fe-foil at 7112 eV. XANES spectra were collected from Fe standards (i.e., FeO, Fe_2O_3 , Fe_3O_4 including a FeCO_3 corrosion film). The lamellae covered areas between 170 and 800 μm^2 . Fluorescence maps (150 maps in total) were collected at discrete energies between 7000 and 7250 eV in raster mode using 2 μm horizontal and 2 μm vertical steps and 0.1s per pixel. The energy points used for fluorescence XANES maps were collected between 7000 and 7100 eV with a resolution of 4.0 eV; between 7100 and 7150 eV the resolution was increased to 0.5 eV, and between 7150 and 7250 eV the resolution was 0.4 eV. To aid with the differentiation of Fe species from the corrosion products and the steel, Mn fluorescence maps were also acquired. An aluminium filter of 0.25 mm was used to attenuate the incident X-ray beam to ensure the linear response of the detector.

For data analysis, fluorescence maps were stacked and converted to a single file containing XANES maps using an in-house python script at the beamline. To analyse the XANES spectral maps, alignment, principal component analysis (PCA) and cluster analysis (CA) were performed in Mantis [42]. Prior PCA and CA analysis, normalisation was performed dividing the intensity value of each spectrum by the last energy point, which yields better speciation cluster analysis rather than intensity differentiation. The number of clusters was determined by using an iterative approach starting with the number of spectral components from PCA and reducing the number of clusters until a local minimum was reached and no further changes on the map were observed as described by Brinza et al 2014 [43].

XANES spectra from Fe standards and those obtained from the cluster analysis were normalized in Athena [44] and compared to the spectra from the clusters obtained in Mantis.

Step size of the XANES spectra from the clusters was 4.0 eV between 7000 and 7100 eV, then 0.5 eV between 7100 eV and 7150 eV, and finally 4.0 eV between 7150 eV and 7250 eV. Spectra of FeCO_3 and Fe_3C obtained from XANES databases were also used for comparison [45, 46]. Linear combination fitting (LCF) between 20 eV below the edge and 30 eV above (i.e., 7092- 7142 eV) was performed to fit the XANES cluster spectra. Weights were constrained to be between 0 and 1, and their sum to be 1. E^0 was not constrained to be the same for all the standards.

Declaration of Competing Interest

The authors declare that they have no known competing financial interests or personal relationships that could have appeared to influence the work reported in this paper.

Supporting Information

The Supporting Information is available free of charge at

Rietveld refinement of diffraction patterns from corrosion films before and after flow experiments; SEM images of cross-sectional views of corrosion films before and after flow experiments; Fe k-edge XANES spectra and LCF of corrosion films (cross-sections) in the range of energy collected; Experimental setup used for the growth of corrosion films on API 5L X65 grade carbon steel (PDF).

Acknowledgements

The authors would like to acknowledge the funding and technical support from BP through the BP International Centre for Advanced Materials (BP-ICAM) which made this research possible. This was financial joint contribution with the EPSRC through the Prosperity partnership grant (EP/R00496X/1). We would like to give special thanks to Prof.

Sarah Haigh and Prof. Sheetal Handa directors of BP-ICAM for their support on this work.

The authors also thank the funding provided from Diamond Light Source through the allocated beamtime on I18 (SP21717-1) and the very helpful support from Konstantin Ignatyev and Kalotina Geraki on spectroscopy data collection. Many thanks to the technical support from the Institute of functional Surfaces at Leeds in addition to Dr Yong Hua for his assistance with autoclave handling. Also, thanks to Mariana Costa Folena and Disha Shaikhah for their help with synchrotron measurements.

References

- [1] Chan, E. W. L. Magnetite and its Galvanic Effect on the Corrosion of Carbon Steel under Carbon Dioxide Environments.; Curtin University, 2011.
- [2] Joshi, G. R.; Cooper, K.; Zhong, X.; Cook, A. B.; Ahmad, E. A.; Harrison, N. M.; Engelberg, D. L.; Lindsay, R., Temporal Evolution of Sweet Oilfield Corrosion Scale: Phases, Morphologies, Habits, and Protection. *Corros. Sci.* **2018**, 142, 110-118.
- [3] Li, W.; Brown, B.; Young, D.; Nešić, S., Investigation of Pseudo-passivation of Mild Steel in CO₂ Corrosion. *Corrosion* **2013**, 70 (3), 294-302.
- [4] Ieamsupapong, S.; Brown, B.; Singer, M.; Nesic, S., Effect of Solution pH on Corrosion Product Layer Formation in a Controlled Water Chemistry System. In *CORROSION 2017*, NACE International: New Orleans, Louisiana, USA, 2017. Paper No. 9160
- [5] Burkle, D.; De Motte, R.; Taleb, W.; Kleppe, A.; Comyn, T.; Vargas, S. M.; Neville, A.; Barker, R., In Situ SR-XRD Study of FeCO₃ Precipitation Kinetics onto Carbon Steel in CO₂-Containing Environments: The Influence of Brine pH. *Electrochimica Acta* **2017**, 255, 127-144.
- [6] Hua, Y.; Barker, R.; Neville, A., Effect of Temperature on the Critical Water Content for General and Localised Corrosion of X65 Carbon Steel in the Transport of Supercritical CO₂. *International Journal of Greenhouse Gas Control* **2014**, 31, 48-60.
- [7] Nesic, S.; Lee, J.; Ruzic, V., A Mechanistic Model of Iron Carbonate Film Growth and the Effect on CO₂ Corrosion of Mild Steel. In *CORROSION 2002*, NACE International: Denver, Colorado, **2002**. Paper No. 2237
- [8] Nešić, S., Key Issues Related to Modelling of Internal Corrosion of Oil and Gas Pipelines – A review. *Corrosion Science* **2007**, 49 (12), 4308-4338.
- [9] Sun, W.; Nešić, S., Kinetics of Corrosion Layer Formation: Part 1—Iron Carbonate Layers in Carbon Dioxide. *Corrosion* **2008**, 64 (4), 334-346.
- [10] Nesic, S.; Wang, S.; Cai, J.; Xiao, Y. Integrated CO₂ Corrosion - Multiphase Flow Model. In *CORROSION 2004*, NACE International: Houston, TX, 2004; Paper No. 04626.
- [11] Pots, B. F. M., Mechanistic Models for the Prediction of CO₂ Corrosion Rates Under Multi-phase Flow Conditions. In *CORROSION 1995*, NACE International: Houston, Texas, **1995**. Paper 137.

- [12] Poulson, B., Complexities in Predicting Erosion Corrosion. *Wear* **1999**, 233-235, 497-504.
- [13] Li, W.; Pots, B. F. M.; Brown, B.; Kee, K. E.; Nesic, S., A Direct Measurement of Wall Shear Stress in Multiphase Flow—Is it an Important Parameter in CO₂ Corrosion of Carbon Steel Pipelines? *Corrosion Science* **2016**, 110, 35-45.
- [14] Schmitt, G.; Gudde, T.; Strobel-Effertz, E., Fracture Mechanical Properties of CO₂ Corrosion Product Scales and their Relation to Localized Corrosion. In *CORROSION 1996*, NACE International: Denver, Colorado, **1996**. Paper 9.
- [15] Ruzic, V.; Veidt, M.; Nesic, S., Protective Iron Carbonate Films Part 2: Chemical Removal by Dissolution in Single-Phase Aqueous Flow. *Corrosion* **2006**, 62 (7), 598-611.
- [16] Ruzic, V.; Veidt, M.; Nešić, S., Protective Iron Carbonate Films—Part 3: Simultaneous Chemo-Mechanical Removal in Single-Phase Aqueous Flow. **2007**, 63 (8), 758-769.
- [17] Yang, Y.; Brown, B.; Nesic, S. Study of Protective Iron Carbonate Layer Dissolution in a CO₂ Corrosion Environment. In *CORROSION 2013*, NACE International, 2013; Paper No. 2708.
- [18] Golubev, S. V.; Bénézech, P.; Schott, J.; Dandurand, J. L.; Castillo, A., Siderite Dissolution Kinetics in Acidic Aqueous Solutions from 25 to 100 °C and 0 to 50 atm pCO₂. *Chemical Geology* **2009**, 265 (1), 13-19.
- [19] Effenberger, H.; Mereiter, K.; Zemmann, J., Crystal Structure Refinements of Magnesite, Calcite, Rhodochrosite, Siderite, Smithonite, and Dolomite, with Discussion of Some Aspects of the Stereochemistry of Calcite Type Carbonates. *Crystalline Materials* **1981**, 156 (3-4), 233-244.
- [20] Ahmad, E. A.; Chang, H.-Y.; Al-Kindi, M.; Joshi, G. R.; Cooper, K.; Lindsay, R.; Harrison, N. M., Corrosion Protection through Naturally Occurring Films: New Insights from Iron Carbonate. *ACS Applied Materials & Interfaces* **2019**, 11 (36), 33435-33441.
- [21] Tanupabrungrun, T.; Young, D.; Brown, B.; Nešić, S., Construction and Verification of Pourbaix Diagrams for CO₂ Corrosion of Mild Steel Valid Up to 250°C. In *CORROSION 2012*, NACE International: Salt Lake City, Utah, **2012**. Paper No. 1418.
- [22] Koziol, A., Carbonate and Magnetite Parageneses as Monitors of Carbon Dioxide and Oxygen Fugacity. *31st Lunar and Planetary Science Conference*, **2000**. Abstract No. 1424.
- [23] Bell, P. E.; Mills, A. L.; Herman, J. S., Biogeochemical Conditions Favoring Magnetite Formation during Anaerobic Iron Reduction. *Appl Environ Microbiol* **1987**, 53 (11), 2610-2616.

- [24] Forero, A. B.; Núñez, M. M. G.; Bott, I. S., Analysis of the Corrosion Scales Formed on API 5L X70 and X80 Steel Pipe in the Presence of CO₂. *J Materials Research* **2014**, *17*, 461-471.
- [25] Zhi-feng, L.; Cao, G.-m.; Lin, F.; Cui, C.-y.; Wang, H.; Liu, Z., Phase Transformation Behavior of Oxide Scale on Plain Carbon Steel Containing 0.4 wt.% Cr during Continuous Cooling. *Transformations and Microstructures*, **2018**, *58* (12), 2338-2347.
- [26] López, D. A.; Schreiner, W. H.; de Sánchez, S. R.; Simison, S. N., The influence of Carbon Steel Microstructure on Corrosion Layers: An XPS and SEM Characterization. *Applied Surface Science* **2003**, *207* (1), 69-85.
- [27] Heuer, J. K.; Stubbins, J. F., An XPS Characterization of FeCO₃ films from CO₂ Corrosion. *Corrosion Science* **1999**, *41* (7), 1231-1243.
- [28] Bruyère, V. I. E.; Blesa, M. A., Acidic and Reductive Dissolution of Magnetite in Aqueous Sulfuric Acid: Site-binding Model and Experimental Results. *Journal of Electroanalytical Chemistry and Interfacial Electrochemistry* **1985**, *182* (1), 141-156.
- [29] Allen, P. D.; Hampson, N. A.; Bignold, G. J., The Electrodissolution of Magnetite: Part II. The oxidation of bulk magnetite. *Journal of Electroanalytical Chemistry and Interfacial Electrochemistry* **1980**, *111* (2), 223-233.
- [30] Mackenzie, R. C., *Differential Thermal Analysis: Fundamental Aspects* New York: Academic Press: 1970; Vol. 1, 327 p.
- [31] Kissinger, H. E.; Mcmurdie, H. F.; Simpson, B. S., Thermal Decomposition of Manganous and Ferrous Carbonates. **1956**, *39* (5), 168-172.
- [32] El-Bellihi, A. A., Kinetics of Thermal Decomposition of Iron Carbonate. *Egyptian Journal of Chemistry* **2010**, *53* (6), 871-884.
- [33] Newville, M., Fundamentals of XAFS. *Reviews in Mineralogy and Geochemistry* **2014**, *78* (1), 33-74.
- [34] Avakyan, L.; Manukyan, A.; Bogdan, A.; Gyulasaryan, H.; Coutinho, J.; Paramonova, E.; Sukharina, G.; Srabionyan, V.; Sharoyan, E.; Bugaev, L., Synthesis and Structural Characterization of Iron-cementite Nanoparticles Encapsulated in Carbon Matrix. *Journal of Nanoparticle Research* **2020**, *22* (1), 30.
- [35] Morard, G.; Boccato, S.; Rosa, A. D.; Anzellini, S.; Miozzi, F.; Henry, L.; Garbarino, G.; Mezouar, M.; Harmand, M.; Guyot, F.; Boulard, E.; Kantor, I.; Irifune, T.; Torchio, R., Solving Controversies on the Iron Phase Diagram Under High Pressure. **2018**, *45* (20), 11074-11082.

- [36] Sha, Z. D.; Quek, S. S.; Pei, Q. X.; Liu, Z. S.; Wang, T. J.; Shenoy, V. B.; Zhang, Y. W., Inverse Pseudo Hall-Petch Relation in Polycrystalline Graphene. *Scientific Reports* **2014**, 4 (1), Paper No. 5991.
- [37] Yu, J.; Wang, M.; Lin, S., Probing the Soft and Nanoductile Mechanical Nature of Single and Polycrystalline Organic–Inorganic Hybrid Perovskites for Flexible Functional Devices. *ACS Nano* **2016**, 10 (12), 11044-11057.
- [38] Burkle, D.; De Motte, R.; Taleb, W.; Kleppe, A.; Comyn, T.; Vargas, S.; Neville, A.; Barker, R., Development of an Electrochemically Integrated SR-GIXRD Flow Cell to Study FeCO₃ Formation Kinetics. *Review of Scientific Instruments* **2016**, 87, 105125-1804.
- [39] Owen, E. A.; Yates, E. L., XLI. Precision Measurements of Crystal Parameters. *The London, Edinburgh, and Dublin Philosophical Magazine and Journal of Science* **1933**, 15 (98), 472-488.
- [40] Schneider, C. A.; Rasband, W. S.; Eliceiri, K. W., NIH Image to ImageJ: 25 Years of Image Analysis. *Nature Methods* **2012**, 9 (7), 671-675.
- [41] Biesinger, M. C.; Payne, B. P.; Grosvenor, A. P.; Lau, L. W. M.; Gerson, A. R.; Smart, R. S. C., Resolving Surface Chemical States in XPS Analysis of First Row Transition Metals, Oxides and Hydroxides: Cr, Mn, Fe, Co and Ni. *Applied Surface Science* **2011**, 257 (7), 2717-2730.
- [42] Lerotic, M.; Mak, R.; Wirick, S.; Meirer, F.; Jacobsen, C., MANTiS: a Program for the Analysis of X-ray Spectromicroscopy Data. *Journal of Synchrotron Radiation* **2014**, 21 (5), 1206-1212.
- [43] Brinza, L.; Schofield, P. F.; Hodson, M. E.; Weller, S.; Ignatyev, K.; Geraki, K.; Quinn, P. D.; Mosselmans, J. F. W., Combining microXANES and microXRD Mapping to Analyse the Heterogeneity in Calcium Carbonate Granules Excreted by the Earthworm *Lumbricus Terrestris*. *Journal of Synchrotron Radiation* **2014**, 21 (1), 235-241.
- [44] Ravel, B.; Newville, M., ATHENA, ARTEMIS, HEPHAESTUS: Data Analysis for X-ray Absorption Spectroscopy Using IFEFFIT. *Journal of Synchrotron Radiation* **2005-2018**, 12 (4), 537-541.
- [45] <http://xraysweb.lbl.gov/uxas/Databases/Overview.htm>. Accessed on 08/06/2020
- [46] <https://cars.uchicago.edu/xaslib/search/Fe>. Accessed on 08/06/2020